


# SHALLOW AU IMPLANTATION INTO SILICON-ON-INSULATOR SLOT RING RESONATOR WAVEGUIDE DEVICES

A PREPRINT

 **Quan-Shan Liu**

Department of Electrical and Electronic Engineering  
Photon Science Institute, University of Manchester  
Oxford Road, Manchester, M13 9PL, UK  
quan-shan.liu@manchester.ac.uk

 **Maddison Coke**

Department of Electrical and Electronic Engineering  
Photon Science Institute, University of Manchester  
Oxford Road, Manchester, M13 9PL, UK  
maddison.coke@manchester.ac.uk

 **Alexander Lincoln**

Faculty of Science and Engineering  
Electron Microscopy Centre, University of Manchester  
Oxford Road, Manchester, M13 9PL, UK  
alexander.lincoln@manchester.ac.uk

 **William Wren**

Department of Electrical and Electronic Engineering  
Photon Science Institute, University of Manchester  
Oxford Road, Manchester, M13 9PL, UK  
william.wren@manchester.ac.uk

 **Tim Echtermeyer**

Department of Electrical and Electronic Engineering  
Photon Science Institute, University of Manchester  
Oxford Road, Manchester, M13 9PL, UK  
tim.echtermeyer@manchester.ac.uk

 **Iain Crowe**

Department of Electrical and Electronic Engineering  
Photon Science Institute, University of Manchester  
Oxford Road, Manchester, M13 9PL, UK  
iain.crowe@manchester.ac.uk

 **Richard J. Curry \***

Department of Electrical and Electronic Engineering  
Photon Science Institute, University of Manchester  
Oxford Road, Manchester, M13 9PL, UK  
richard.curry@manchester.ac.uk

## ABSTRACT

The optical transmission spectra of a series of micro-ring resonators (MRRs) are studied following the implantation of gold (Au) ions and subsequent thermal annealing, at temperatures between 500 °C and 700 °C. Whilst we find that this process leads to the ready formation of Au nanoparticles (NPs) on the MRR surface, the cavity optical properties; Q-factor and extinction ratio (ER) are severely degraded, for annealing between 500 °C and 600 °C, but recover again for annealing at 650 °C. For an equivalent (control) MRR, which received no Au implantation, thermal annealing alone was also found to degrade the cavity performance.

## 1 Introduction

Silicon-based photonic devices have been a focus of intense research over recent decades, due to their compatibility with the prevailing complementary metal-oxide-semiconductor (CMOS) fabrication technology[Siew et al., 2021, Xiang et al., 2021, Lim et al., 2013, Baehr-Jones et al., 2012, Soref, 2006]. Compared with other silicon photonics platforms such as silicon nitride[Hu et al., 2017], silicon-on-sapphire[Baehr-Jones et al., 2010], suspended silicon[Cheng et al., 2012], and chalcogenides-on-silicon[Ma et al., 2013], silicon-on-insulator (SOI) is the most mature and widely offered by a number of foundries[Siew et al., 2021]. As a result, researchers have developed a variety of SOI-based photonic

\*The corresponding author.

building blocks[Maharjan et al., 2021, Poudel et al., 2023], among which microring resonators (MRRs) are well characterised and have been applied as functional sensors[Kazanskiy et al., 2023, Yebo et al., 2009, Kim and Yu, 2016, Zhang et al., 2016, TalebiFard et al., 2017, Lo et al., 2017, Rodriguez et al., 2015, Kim et al., 2010, De Vos et al., 2007], including via 2D materials integration[Hussein et al., 2017, Crowe et al., 2014, Leo Tsui et al., 2020], and more recently for the realization of novel, non-Hermitian photonics-based Parity-Time (P-T) symmetry structures[Li et al., 2024a,b]. Furthermore, the slot waveguide geometry has been introduced into MRRs for achieving enhanced light-matter interaction and thus improving sensing performance[Robinson et al., 2008, Liu et al., 2013, Barrios et al., 2008, Claes et al., 2009].

The utilization of ion implantation techniques opens additional possibilities for the modification of material functionality[Namba and Masuda, 1975]. This technique can be readily incorporated into CMOS processing with minimum impact on device fabrication[Jacobson et al., 1995]. Through the introduction of selected atomic species with well-defined doses and selected depths, implanted matrices may display novel properties. In particular, gold has been widely implanted into a range of targets including silicon wafers[Mailoa et al., 2014, Hashim et al., 2013], sapphire[Stepanov et al., 2005], silicate glasses[Malinský et al., 2009], Nd: YAG crystals[Nie et al., 2018], TiO<sub>2</sub> crystal[Ye et al., 2022], LiTaO<sub>3</sub> crystals[Pang et al., 2021], silica[Magruder III et al., 1993, Torres-Torres et al., 2015], and polymethyl methacrylate resist[Adshead et al., 2023]. It has been observed that with suitable post-implantation annealing Au nanoparticles (NPs) may be formed displaying plasmonic properties [Nie et al., 2018, Wang et al., 2024, Ribeiro et al., 2023, Hsieh et al., 2016, Ramaswamy et al., 2005]. However, gold implantation directly into MRRs has remained unexplored, though some attention has been paid to other dopants including oxygen[Waldow et al., 2008], germanium[Reed et al., 2017, Milosevic et al., 2018], silicon[Ackert et al., 2011], and boron[Ackert et al., 2011, Hagan et al., 2019].

In this paper we report experimental studies of gold implantation into SOI-based slot MRRs with the aim of Au NP formation and modification of the MRR optical response. The transmission spectra of MRR devices at each stage of processing (pre/post-implant and post-annealing) are measured to obtain extinction ratios (ER) and quality factors (QF) to assess the impact of the processing. Though in this study we found no evidence of any enhanced plasmonic effect associated with the coupling of Au NPs to the MRRs, the impact of the processing on the MRR optical response is elucidated.

## 2 Sample details and methods

All the waveguide devices studied were rib-type and designed for single-mode operation around 1550 nm. Based on a commercial 220 nm SOI platform, the rib waveguides were on-chip fabricated by deep ultraviolet lithography, with a 130 nm rib height and 90 nm slab thickness on top of a 2  $\mu$ m buried oxide layer. The chip was coated with silica cladding of  $\sim 1.5$   $\mu$ m thickness for device protection.

### 2.1 Device structure and ion implantation

The slot MRRs used in this study can be classified into two configurations consisting of (i) ‘single-input-through’ and (ii) ‘add-drop’ designs. Figures 1a to 1c show schematic plan-views of three add-drop slot MRRs, with the structural parameters defined as follows: inner ring waveguide width  $w_{in} = 290$  nm; outer ring waveguide width  $w_{out} = 250$  nm; nearby bus waveguide width  $w_{bus} = 320$  nm; ring-to-ring gap  $g_{ring} = 200$  nm; ring-to-bus gap  $g_c = 200$  nm, 250 nm, and 300 nm for Figures 1a to 1c respectively; and radius to slot centre  $r_{ring} = 25$   $\mu$ m. To allow ion implantation into the MRRs a series of  $64 \mu\text{m} \times 35 \mu\text{m}$  etched windows were opened through the silica capping layer, shown by the green box in Figure 1a-c and visible in the optical images in Figure 1d-f. The slot MRR device in Figure 1a remained unimplanted as a reference (referred to as device A); the two devices in Figure 1b and 1c were implanted with 25 keV Au<sup>+</sup> ions into a region covering  $\sim 18\%$  (Figure 1b, device B) and  $\sim 46\%$  (Figure 1c, device C) of the total MRR with a dose of  $5 \times 10^{14}$  ions/cm<sup>2</sup>. Device C appears to have a discontinuity in its ring that was not noticed prior to characterization. Surprisingly, resonances are still measurable for this “incomplete-ring” structure, with wider peak widths compared to those of devices A and B (to be shown in later figure).

A second set of single bus MRR devices were likewise implanted for study, again one of these single-input slot MRR devices remained unimplanted providing a reference (referred to as device D). The two other devices (referred to as devices E and F respectively) were implanted with 25 keV Au<sup>+</sup> ions into a region covering  $\sim 22\%$  and  $\sim 49\%$  of the total MRR respectively, with a higher dose of  $1 \times 10^{15}$  ions/cm<sup>2</sup>. The percentages of coverage are calculated based on the implantation areas presented in the optical figures, and the details of implantation of all the devices mentioned are summarized in Table 1.

The ion implantation was performed using the platform for nanoscale advanced materials engineering (P-NAME) Facility (Ionoptika, Q-One) at the University of Manchester[Adshead et al., 2023]. Inspection of the optical microscope

Table 1: Summary of implantation details for each device.

Device	Implantation dose (ions/cm <sup>2</sup> )	Comments
A	-	add-drop; reference device
B	5E14	add-drop; covering ~18% of the total MMR
C	5E14	add-drop; covering ~46% of the total MMR
D	-	single-input; reference device
E	1E15	single-input; covering ~22% of the total MMR
F	1E15	single-input; covering ~49% of the total MMR

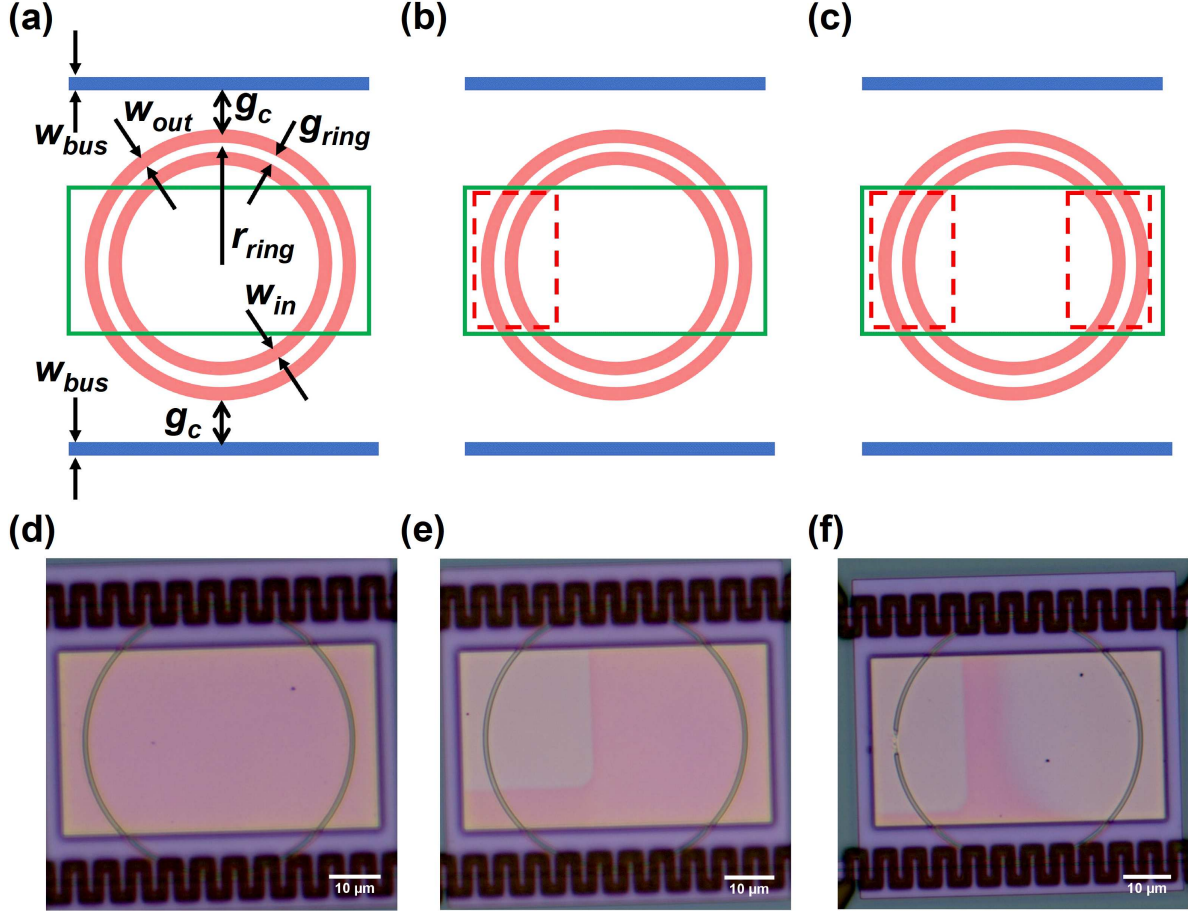


Figure 1: (a) to (c) Plan-view not to scale schematic illustration of three add-drop slot MRR devices with the device design parameters defined (values provided in the text). The blue lines represent the bus waveguides adjacent to the MRRs shown in pink. The etched cladding region is shown by the green box with the red dashed boxes indicating the regions implanted with Au ions. (d) to (f) Optical microscope images of each device post-implantation corresponding to (a) to (c). The implanted area is observed as the colourless region contrasting with the pink-tinged unimplanted regions.

images exhibits a clear contrast between implanted and unimplanted areas (clear and pink), illustrated in Figure 1d to 1f for devices A to C respectively. Post-implantation thermal annealing is typically required for both repairing ion damage and electronic activation of implanted dopants[Mayer et al., 1970]. The selection of optimal annealing conditions is highly empirical and varies depending on the specific implanted species and the host material. In this case the temperature and duration must be sufficient to stimulate the migration of the implanted Au ions to form NPs whilst not resulting in damage to the waveguides. In order to determine a starting point for annealing whilst preserving MRRs, 25 kV Au<sup>+</sup> was first implanted, at a dose of 5E15 ions/cm<sup>2</sup>, into a simple on-chip linear waveguide along a 500  $\mu$ m length. Annealing was then performed under a nitrogen atmosphere at 500  $^{\circ}$ C.

To ascertain that these annealing conditions are suitable for the formation of Au NPs SEM imaging of the implanted waveguides was undertaken (Supplementary Information, Figures S1a and S1b). Close inspection revealed the formation of Au NPs with a diameter of  $\sim 10$  nm on the sample surface. Energy dispersive x-ray spectroscopy (EDS) was used to compare waveguides with and without Au implantation with an enhancement of the Au x-ray signal observed (Supplementary Information, Figure S1c) in the implanted area. These results indicated that a 500 °C anneal is a suitable temperature to initiate Au NP formation however, this alone may not be sufficient to repair implantation damage. To assess this the transmission spectra of the linear waveguide were measured pre- and post-implantation and again post-anneal. It is found that implantation leads to sufficient damage to prevent waveguiding which is not recovered by a 500 °C anneal.

To study the MRR devices A to F (Table 1) a series of thermal anneals were performed under a nitrogen atmosphere each lasting for 2 minutes at temperatures between 500 °C to 700 °C at 50 °C increments, summarised in Table 2. The two unimplanted reference devices (A and D) were also subject to the same thermal annealing.

Table 2: Summary of annealing cycles undertaken.

Stage	Definition	Comments
1	Pre-implant	-
2	Post-implant	Devices A and D remained unimplanted
3	Post-anneal under 500 °C	N <sub>2</sub> atmosphere for 2 minutes
4	Post-anneal under 550 °C	N <sub>2</sub> atmosphere for 2 minutes
5	Post-anneal under 600 °C	N <sub>2</sub> atmosphere for 2 minutes
6	Post-anneal under 650 °C	N <sub>2</sub> atmosphere for 2 minutes
7	Post-anneal under 700 °C	N <sub>2</sub> atmosphere for 2 minutes

Following each stage MRR characterisation was performed, described below, and post stage 7 SEM images of devices C and F were obtained (Figure 2). Within each image sporadic Au NP decoration can be observed, increasing in density with Au dose (5E14 and 1E15 ions/cm<sup>2</sup> for devices C and F respectively). Alongside this, EDS analysis was performed on the implanted and unimplanted areas of devices B and E (Supplementary Information, Figures S2a and S2b) showing an increase of the Au signal in the implanted regions.

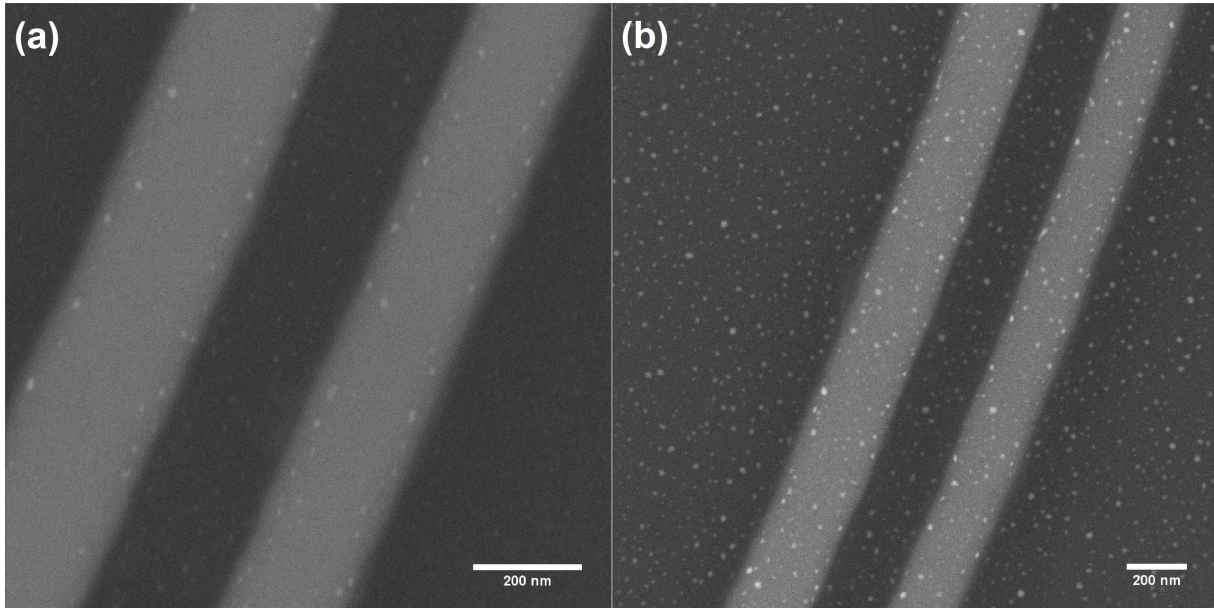


Figure 2: (a) Back scattered electron image for the implanted ring waveguide of device C. (b) back scattered electron image for the implanted ring waveguide of device F. Both devices have gone through a number of 2 min thermal anneals between 500 °C and 700 °C at 50 °C intervals (stages 1 to 7 in Table 2).

### 3 Experimental set-up

To quantify the impact of the Au implantation and thermal annealing on the MMR devices the transmission of each device's bus waveguide was measured at each stage of processing. For the add-drop slot MRRs, the same bus waveguide was consistently selected for characterization after each stage. A Thorlabs 1550 nm fibre-coupled benchtop superluminescent diode coupled to a single-mode cleaved-end fibre was used to launch light into the waveguide via the predefined grating couplers. Transmitted light was similarly collected using a multi-mode fibre and inserted into an Anritsu optical spectrum analyser. All measurements were taken at room temperature and over the 1450 nm to 1650 nm spectral range.

The measured input and output wavelength dependent power ( $P_{in}$  and  $P_{out}$  respectively) is used to obtain the transmission loss of waveguides (including input and output grating couplers), as:

$$Loss = 10 \times \log_{10}(P_{out}/P_{in}) \quad (1)$$

Figure 3a shows the  $P_{in}$  and  $P_{out}$  of the unimplanted reference device A during one measurement. Each spectrum was collected three times, performing a fresh fibre alignment each time, to obtain the mean value and standard deviation.

### 4 Data processing and analysis

In Figure 3a, the grating coupler bandwidth is not in perfect alignment with the light source. Nevertheless, resonant patterns are observed both below and above 1550 nm. As such, two selected regions (1455 to 1545 nm, and 1570 to 1610 nm) of each measured spectra were chosen for data processing and analysis, each displaying multiple resonance peaks. The processing removed the background response within the selected regions using subtraction of a polynomial fit resulting in a flattening of the spectrum, Figure 3b and 3c. This step does not change any resonance properties and is helpful for resonance comparison among different spectra. The ER and QF were derived from Lorentzian fitting of the resonance peaks based on the least square method using MATLAB codes modified from that provided in reference [Alsaman, 2021].

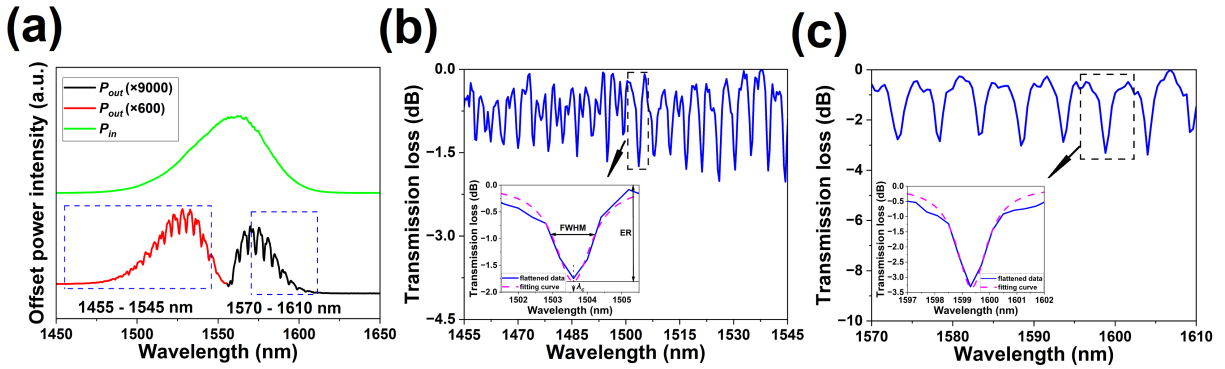


Figure 3: (a) The input and output power intensity of reference device A as received (vertically offset for clarity). The two selected regions over which background subtraction and analysis was performed are shown enclosed by blue dashed boxes. (b) and (c) Demonstration of spectrum flattening and resonance peak fitting for the two selected regions displayed in (a).

Figures 3b and 3c show the flattened data (blue line) and the fitted Lorentzian curves to one resonance (magenta dashed line) for the two marked regions in Figure 3a. Relevant parameters including one peak's ER, full-width half maximum (FWHM), and central resonant wavelength ( $\lambda_c$ ) are illustrated in Figure 3b inset. Separate spectrum flattening and curve fitting is completed for the two selected wavelength regions. To ensure consistent convergence of peak fitting, only resonances exceeding 70% of the deepest resonance peak in each region are selected for fitting.

## Results and discussion

### 4.1 Transmission spectrum analysis

Figures 4a to 4f show the flattened resonance peaks of devices A to F (Table 1) respectively at all stages of processing (see Table 2 for stage definition). The transmission of devices B, D, E, and F following stage 7 (700 °C annealing) are not included as these devices exhibited no transmission. This clearly indicates device failure resulting from thermally induced damage caused by thermal expansion coefficient mismatch between the Si and SiO<sub>2</sub>. Damage can be visibly observed by comparing optical microscope images of the devices following stage 1, 6, and 7 (Supplementary Information, Figure S3).

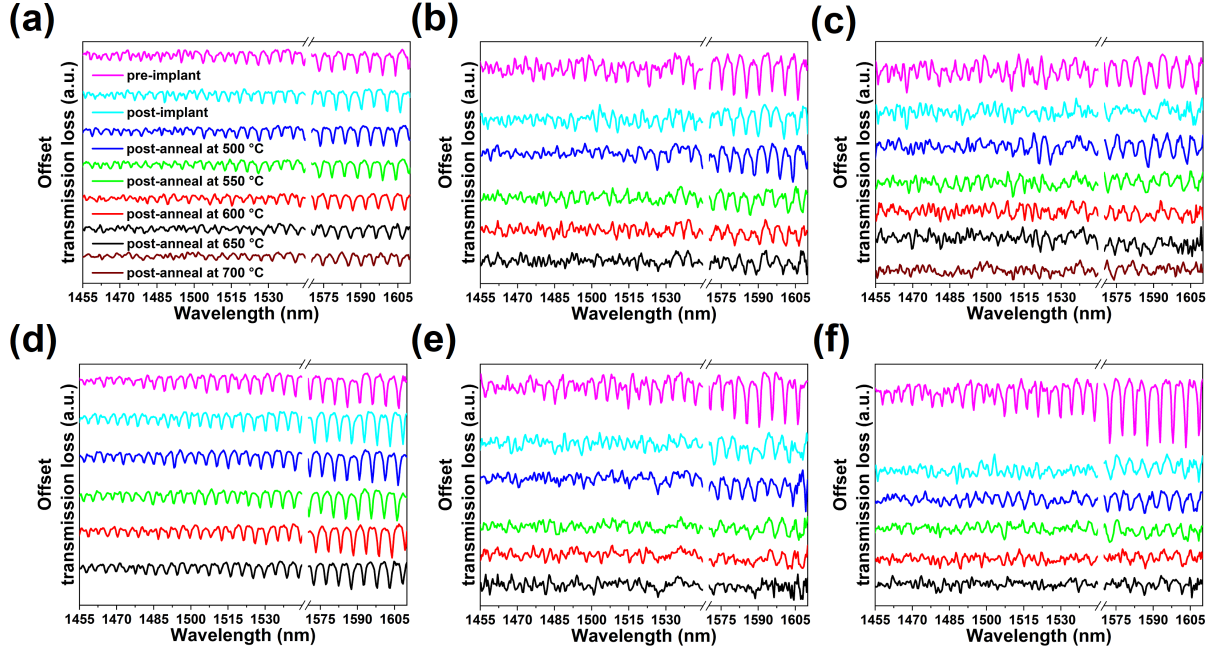


Figure 4: (a) to (f) Flattened transmission spectra of devices A to F respectively. Within each panel the stages progress from top (stage 1) to bottom as indicated in (a) and are vertically offset for clarity.

Following implantation (stage 2) but prior to any annealing, all implanted devices experience a reduced coupling to the MRR with devices C and F (higher doses) reducing more than devices B and E (lower doses). The QFs of both of the unimplanted reference devices are also found to be slightly different which might be attributed to variation in laboratory conditions (e.g. humidity) between measurements. Following 500 °C annealing it is observed that the MRR resonance peaks have recovered somewhat, indicating a reduction in ion-induced damage. Additionally, at this temperature Au ions have diffused out of the waveguides to form Au NPs on the device surface as shown in Figure 2. Annealing at higher temperature (stages 3 to 7) results in a general degradation of the MRR ER. For the reference unimplanted devices, a slight degradation in MRR QF can be seen as annealing progresses. To quantify the above outlined impact of annealing on the devices Lorentz fitting of the resonance peaks was performed.

### 4.2 Extinction ratio analysis

To extract ERs from the resonance peaks displayed in Figure 4, Lorentz curve fitting was performed as described above. Figure 5 displays the average ER within each wavelength region analysed for each of the different experimental stages performed, with error bars representing the standard deviation.

As shown in Figure 5a and 5b, the average ERs measured across the 1455 nm to 1545 nm region of devices B, C, E, and F reduce by 20%, 24%, 38%, and 39% following implantation. A similar trend is displayed within the 1570 nm to 1610 nm region, Figure 5c and 5d, but with greater reduction of the ERs by 25%, 36%, 47%, and 66% for devices B, C, E, and F respectively. The reduction in ER increases with implantation dose and area, strongly linking it to ion implantation induced damage within the MRRs. Annealing at 500 °C does not repair this damage as mentioned above for the test linear waveguide, however Au NPs are formed on the MRR surface. Inspection of the bus waveguide

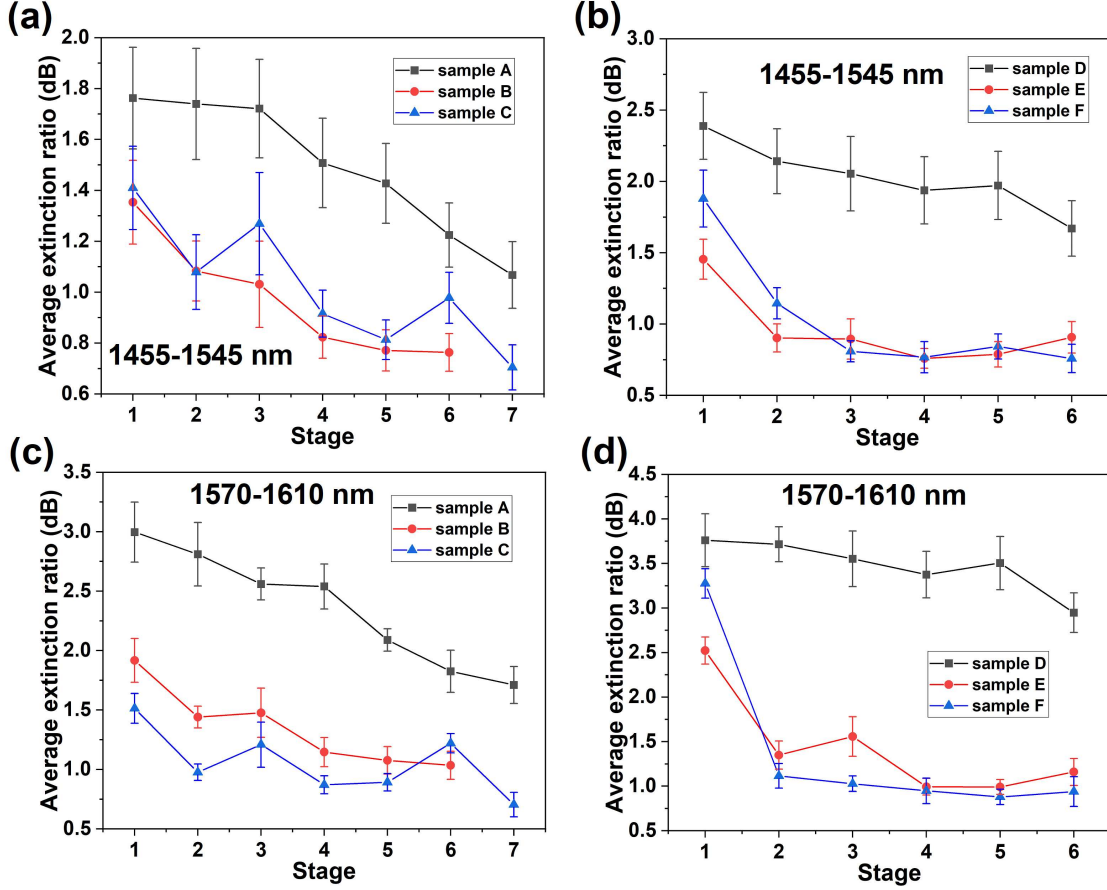


Figure 5: The average ERs of (a) devices A to C in the 1455 to 1545 nm region, (b) devices D to F in the 1455 to 1545 nm region, (c) devices A to C in the 1570 to 1610 nm region and (d) devices D to F in the 1570 to 1610 nm region following each experimental stage (Table 2).

transmission spectra before and after implantation, and following 500 °C annealing, did not reveal any obvious spectral difference in response. Plasmonic coupling to the Au NPs surface plasmon modes is ruled out as the wavelengths used are not in resonance with the Au surface plasmon energy ( 515 nm to 570 nm for 10 nm to 100 nm diameter NPs respectively).

To see if higher annealing temperatures can be effective in recovering performance the further sequential anneals were performed up to 700 °C. Following each of the subsequent annealing stages the ERs of both of the unimplanted reference devices exhibit a steady reduction. Those of the implanted devices B and C likewise continue to decline with post implantation annealing. In contrast the ERs of devices E and F appear to remain similar to their post implantation values. High-temperature annealing is expected to lead to some structural deformation due to the thermal expansion coefficient mismatch within the chip resulting in increased loss. However, annealing also recovers ion-induced damage and can lead to surface smoothing which should reduce loss. These effects are in competition and would appear to be balanced for devices E and F.

### 4.3 Quality factor analysis

The quality factor (QF) is defined as the ratio of the central resonant wavelength to the full-width half maximum of the resonance. High QFs are usually desired to realise ultra-sensitive photonic devices. QFs were extracted from the Lorentzian fits to the resonance peaks shown in Figure 4. Figure 6 presents the average QFs of each device at each experimental stage, with the error bars indicating the standard deviations.

The variation of the QFs with implantation and annealing is not as obvious as that of the ERs with most variation occurring within the measurement error confidence. For the unimplanted devices, Figures 6a and 6b suggest that the

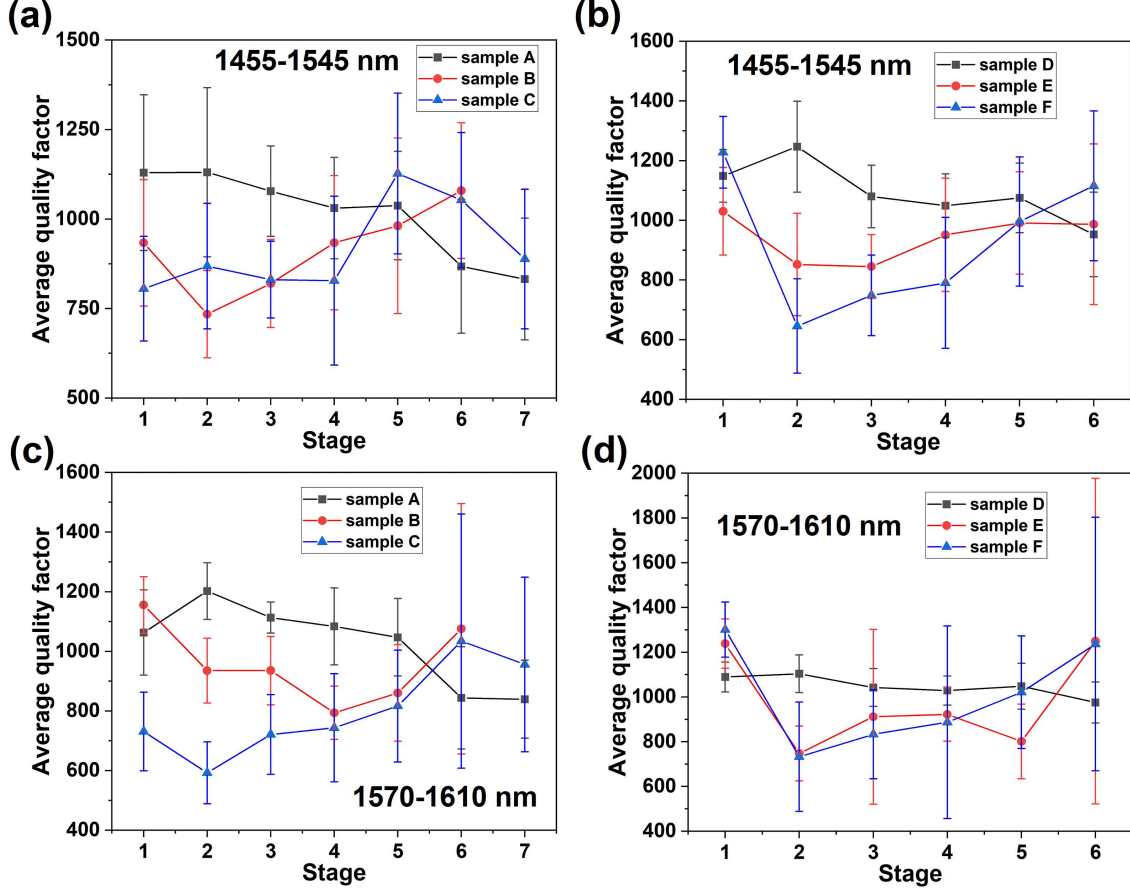


Figure 6: The average QFs of (a) devices A to C in the 1455 to 1545 nm region, (b) devices D to F in the 1455 to 1545 nm region, (c) devices A to C in the 1570 to 1610 nm region and (d) devices D to F in the 1570 to 1610 nm region following each experimental stage (Table 2).

QF of reference device A undergoes only a small reduction until an obvious decrease at stage 6 (annealing at 650 °C). The QF of reference device D is barely affected by annealing. Following ion implantation, a clear reduction in QF is generally observed for all devices as shown in Figure 6. There appears to be no strong relationship between the magnitude of the QF reduction and implantation dose or area. As annealing proceeds up to 650 °C, the overall outcome is for the QFs of implanted devices to return to a similar value as that measured pre-implantation. Further annealing at a higher temperature (700 °C, stage 7) does not seem to result in any further QF increase but did damage several devices. Further analysis is impeded by relatively large error bars which are possibly caused by the uneven distribution of peak widths indicated in Figure 4.

## 5 Conclusion

We have explored the feasibility of forming Au NPs on the surface of SOI slot MRR waveguides through the use of FIB implantation. The presence of the Au NPs following 25 keV Au implantation at doses of  $5E14$  and  $1E15$  ions/cm<sup>2</sup> and following a 500 °C thermal anneal was verified via SEM imaging and EDS analysis. The impact of ion implantation on the waveguiding properties of the MRR systems is to reduce their cavity ER and QF, as would be expected due to ion induced damage. Thermal annealing alone, at temperatures from 500 °C to 700 °C, is also observed to result in a reduction of the waveguiding and MRR performance indicating that damage is occurring which we attribute to thermal expansion mismatch within the structures. Annealing of the Au implanted devices is found to result in a further reduction in waveguiding as measured by the ERs of the measured devices. In contrast annealing at a temperature of 650 °C was able to almost fully recover the measured QFs of implanted devices. Whilst this work demonstrated the ability to form Au NPs through direct writing of Au ions into MMR devices, the resulting optical properties are degraded by both the implantation itself and the thermal treatment.

## 6 Acknowledgements

This work was funded by EPSRC grant EP/V001914/1, and by capital investment by the University of Manchester. Q-S.L thanks the China Scholarship Council for financial support.

## 7 Author contributions statement

Q-S.L, M.C, A.L, and W.W conducted all experimental work. Q-S.L, M.C and R.C performed data analysis. T.E, I.C and R.C supervised the work. All authors contributed to the writing of the manuscript.

## 8 Competing interests

The author(s) declare no competing interests.

## References

- Shawn Yohanes Siew, Bo Li, Feng Gao, Hai Yang Zheng, Wenle Zhang, Pengfei Guo, Shawn Wu Xie, Apu Song, Bin Dong, Lian Wee Luo, et al. Review of silicon photonics technology and platform development. *Journal of Lightwave Technology*, 39(13):4374–4389, 2021.
- Chao Xiang, Steven M Bowers, Alexis Bjorlin, Robert Blum, and John E Bowers. Perspective on the future of silicon photonics and electronics. *Applied Physics Letters*, 118(22), 2021.
- Andy Eu-Jin Lim, Junfeng Song, Qing Fang, Chao Li, Xiaoguang Tu, Ning Duan, Kok Kiong Chen, Roger Poh-Cher Tern, and Tsung-Yang Liow. Review of silicon photonics foundry efforts. *IEEE Journal of Selected Topics in Quantum Electronics*, 20(4):405–416, 2013.
- Tom Baehr-Jones, Thierry Pinguet, Patrick Lo Guo-Qiang, Steven Danziger, Dennis Prather, and Michael Hochberg. Myths and rumours of silicon photonics. *Nature Photonics*, 6(4):206–208, 2012.
- Richard Soref. The past, present, and future of silicon photonics. *IEEE Journal of selected topics in quantum electronics*, 12(6):1678–1687, 2006.
- Ting Hu, Bowei Dong, Xianshu Luo, Tsung-Yang Liow, Junfeng Song, Chengkuo Lee, and Guo-Qiang Lo. Silicon photonic platforms for mid-infrared applications. *Photonics Research*, 5(5):417–430, 2017.
- Tom Baehr-Jones, Alexander Spott, Rob Ilic, Andrew Spott, Boyan Penkov, William Asher, and Michael Hochberg. Silicon-on-sapphire integrated waveguides for the mid-infrared. *Optics express*, 18(12):12127–12135, 2010.
- Zhenzhou Cheng, Xia Chen, Chi Yan Wong, Ke Xu, and Hon Ki Tsang. Mid-infrared suspended membrane waveguide and ring resonator on silicon-on-insulator. *IEEE photonics journal*, 4(5):1510–1519, 2012.
- Pan Ma, Duk-Yong Choi, Yi Yu, Xin Gai, Zhiyong Yang, Sukanta Debbarma, Steve Madden, and Barry Luther-Davies. Low-loss chalcogenide waveguides for chemical sensing in the mid-infrared. *Optics express*, 21(24):29927–29937, 2013.
- Rijan Maharjan, Sanket Bohora, Pravin Bhattarai, Iain Crowe, Richard J Curry, Richard Hogg, David Childs, and Ashim Dhakal. Non-diffracting beam generated from a photonic integrated circuit based axicon-like lens. *Optics Express*, 29(7):10480–10490, 2021.
- Ankit Poudel, Pravin Bhattarai, Rijan Maharjan, Maddison Coke, Richard J Curry, Iain F Crowe, and Ashim Dhakal. Spectrometer based on a compact disordered multi-mode interferometer. *Optics Express*, 31(8):12624–12633, 2023.
- Nikolay L Kazanskiy, Svetlana N Khonina, and Muhammad A Butt. A review of photonic sensors based on ring resonator structures: three widely used platforms and implications of sensing applications. *Micromachines*, 14(5):1080, 2023.
- Nebiyu Adello Yebo, Dirk Taillaert, Joris Roels, D Lahem, M Debligny, Dries Van Thourhout, and Roel Baets. Silicon-on-insulator (soi) ring resonator-based integrated optical hydrogen sensor. *IEEE photonics technology letters*, 21(14):960–962, 2009.
- Hyun-Tae Kim and Miao Yu. Cascaded ring resonator-based temperature sensor with simultaneously enhanced sensitivity and range. *Optics Express*, 24(9):9501–9510, 2016.
- G Zhang, X L Feng, B Liedberg, and A Q Liu. Gas sensor for volatile organic compounds detection using silicon photonic ring resonator. *Procedia Engineering*, 168:1771–1774, 2016.

- Sahba TalebiFard, Shon Schmidt, Wei Shi, Wen Xuan Wu, Nicolas AF Jaeger, Ezra Kwok, Daniel M Ratner, and Lukas Chrostowski. Optimized sensitivity of silicon-on-insulator (soi) strip waveguide resonator sensor. *Biomedical optics express*, 8(2):500–511, 2017.
- Stanley M Lo, Shuren Hu, Girija Gaur, Yiorgos Kostoulas, Sharon M Weiss, and Philippe M Fauchet. Photonic crystal microring resonator for label-free biosensing. *Optics express*, 25(6):7046–7054, 2017.
- Gilberto A Rodriguez, Shuren Hu, and Sharon M Weiss. Porous silicon ring resonator for compact, high sensitivity biosensing applications. *Optics express*, 23(6):7111–7119, 2015.
- Gun-Duk Kim, Hak-Soon Lee, Chang-Hyun Park, Sang-Shin Lee, Boo Tak Lim, Hee Kyoung Bae, and Wan-Gyu Lee. Silicon photonic temperature sensor employing a ring resonator manufactured using a standard cmos process. *Optics express*, 18(21):22215–22221, 2010.
- Katrien De Vos, Irene Bartolozzi, Etienne Schacht, Peter Bienstman, and Roel Baets. Silicon-on-insulator microring resonator for sensitive and label-free biosensing. *Optics express*, 15(12):7610–7615, 2007.
- Siham M Hussein, Iain F Crowe, Nick Clark, Milan Milosevic, Aravind Vijayaraghavan, Frederic Y Gardes, Goran Z Mashanovich, and Matthew P Halsall. Raman mapping analysis of graphene-integrated silicon micro-ring resonators. *Nanoscale Research Letters*, 12:1–8, 2017.
- Iain F Crowe, Nicholas Clark, Siham Hussein, Brian Towlson, Eric Whittaker, Milan M Milosevic, Frederic Y Gardes, Goran Z Mashanovich, Matthew P Halsall, and Aravind Vijayaraghavan. Determination of the quasi-te mode (in-plane) graphene linear absorption coefficient via integration with silicon-on-insulator racetrack cavity resonators. *Optics express*, 22(15):18625–18632, 2014.
- HC Leo Tsui, Osamah Alsaman, Boyang Mao, Abdullah Alodhayb, Hamad Albrithen, Andrew P Knights, Matthew P Halsall, and Iain F Crowe. Graphene oxide integrated silicon photonics for detection of vapour phase volatile organic compounds. *Scientific Reports*, 10(1):9592, 2020.
- Tianrui Li, Matthew P Halsall, and Iain F Crowe. N-order generalized-temporal coupled mode theory (g-tcmt) model: extending the spectral range for arbitrary coupling of optical resonators and application in parity-time (pt) symmetry. *Optics Express*, 32(26):46569–46577, 2024a.
- Tianrui Li, Matthew P Halsall, and Iain F Crowe. Modeling the non-hermitian infinity-loop micro-resonator over a free spectral range reveals the characteristics for operation at an exceptional point. *Symmetry*, 16(4):430, 2024b.
- Jacob T Robinson, Long Chen, and Michal Lipson. On-chip gas detection in silicon optical microcavities. *Optics Express*, 16(6):4296–4301, 2008.
- Qing Liu, Xiaoguang Tu, Kyung Woo Kim, Jack Sheng Kee, Yong Shin, Kyungsup Han, Yong-Jin Yoon, Guo-Qiang Lo, and Mi Kyoung Park. Highly sensitive mach–zehnder interferometer biosensor based on silicon nitride slot waveguide. *Sensors and Actuators B: Chemical*, 188:681–688, 2013.
- Carlos A Barrios, Maria Jose Banuls, Victoria Gonzalez-Pedro, Kristinn B Gylfason, Benito Sanchez, Amadeu Griol, Angel Maquieira, Hans Sohlström, Miquel Holgado, and Rafael Casquel. Label-free optical biosensing with slot-waveguides. *Optics letters*, 33(7):708–710, 2008.
- Tom Claes, Jordi Girones Molera, Katrien De Vos, Etienne Schacht, Roel Baets, and Peter Bienstman. Label-free biosensing with a slot-waveguide-based ring resonator in silicon on insulator. *IEEE Photonics journal*, 1(3):197–204, 2009.
- Susumu Namba and Kohzoh Masuda. Ion implantation in semiconductors. In *Advances in Electronics and Electron Physics*, volume 37, pages 263–330. Elsevier, 1975.
- D C Jacobson, A Kamgar, D J Eaglesham, E J Lloyd, S J Hillenius, and J M Poate. High energy ion implantation for profiled tub formation and impurity gettering in deep submicron cmos technology. *Nuclear Instruments and Methods in Physics Research Section B: Beam Interactions with Materials and Atoms*, 96(1-2):416–419, 1995.
- Jonathan P Mailoa, Austin J Akey, Christie B Simmons, David Hutchinson, Jay Mathews, Joseph T Sullivan, Daniel Recht, Mark T Winkler, James S Williams, Jeffrey M Warrender, et al. Room-temperature sub-band gap optoelectronic response of hyperdoped silicon. *Nature communications*, 5(1):3011, 2014.
- Nur ZI Hashim, Ahmed Abuelgasim, and Cornelis H de Groot. Coplanar waveguides on gold-doped high resistivity silicon for 67-ghz microwave application. In *2013 IEEE International RF and Microwave Conference (RFM)*, pages 274–277. IEEE, 2013.
- A L Stepanov, C Marques, E Alves, RC Da Silva, M R Silva, R A Ganeev, AI Ryasnyansky, and T Usmanov. Nonlinear optical properties of gold nanoparticles synthesized by ion implantation in sapphire matrix. *Technical physics letters*, 31:702–705, 2005.

- P Malinský, A Macková, J Bočan, B Švecová, and P Nekvindová. Au implantation into various types of silicate glasses. *Nuclear Instruments and Methods in Physics Research Section B: Beam Interactions with Materials and Atoms*, 267(8-9):1575–1578, 2009.
- W J Nie, Y X Zhang, H H Yu, Rang Li, R Y He, N N Dong, Jun Wang, René Hübner, Roman Böttger, S Q Zhou, et al. Plasmonic nanoparticles embedded in single crystals synthesized by gold ion implantation for enhanced optical nonlinearity and efficient q-switched lasing. *Nanoscale*, 10(9):4228–4236, 2018.
- Qingchuan Ye, Chi Pang, Han Zhu, Rang Li, and Feng Chen. Embedded gold nanoparticles in tio2 crystal for photonic applications. *Materials Letters*, 326:132995, 2022.
- Chi Pang, Rang Li, Ziqi Li, Xiaoli Sun, Ningning Dong, Jun Wang, Shengqiang Zhou, and Feng Chen. Q-switched mode-locked laser generation by au nanoparticles embedded in litao3 crystals. *Optical Materials*, 122:111714, 2021.
- R H Magruder III, Li Yang, R F Haglund Jr, C W White, Lina Yang, R Dorsinville, and R R Alfano. Optical properties of gold nanocluster composites formed by deep ion implantation in silica. *Applied physics letters*, 62(15):1730–1732, 1993.
- Carlos Torres-Torres, A López-Suárez, B Can-Uc, R Rangel-Rojo, L Tamayo-Rivera, and A Oliver. Collective optical kerr effect exhibited by an integrated configuration of silicon quantum dots and gold nanoparticles embedded in ion-implanted silica. *Nanotechnology*, 26(29):295701, 2015.
- Mason Adshead, Maddison Coke, Gianfranco Aresta, Allen Bellew, Matija Lagator, Kexue Li, Yi Cui, Rongsheng Cai, Abdulwahab Almutawa, Sarah J Haigh, et al. A high-resolution versatile focused ion implantation platform for nanoscale engineering. *Advanced Engineering Materials*, 25(22):2300889, 2023.
- Hongpei Wang, Hao Dai, Menglu Lyu, Cheng Jiang, Shulong Lu, and Ziyang Zhang. Effects of plasmonic au nanoparticles on the optical nonlinearity of inas/gaas quantum dot semiconductor saturable absorber mirrors. In *Photonics*, volume 11, page 235. MDPI, 2024.
- A Ribeiro, M Proença, N Catarino, M Dias, M Peres, J Borges, F Vaz, and E Alves. Plasmonic au nanoparticles by ion implantation. *Nuclear Instruments and Methods in Physics Research Section B: Beam Interactions with Materials and Atoms*, 541:336–341, 2023.
- Chang-Lin Hsieh, Keiji Oyoshi, Der-Sheng Chao, Hsu-Sheng Tsai, Wei-Lun Hong, Yoshihiko Takeda, and Jenq-Hong Liang. Optical properties of ion-beam-synthesized au nanoparticles in sio2 matrix. *Nuclear Instruments and Methods in Physics Research Section B: Beam Interactions with Materials and Atoms*, 375:56–59, 2016.
- Vidya Ramaswamy, Tony E Haynes, C Woody White, Warren J MoberlyChan, Sjoerd Roorda, and Michael J Aziz. Synthesis of nearly monodisperse embedded nanoparticles by separating nucleation and growth in ion implantation. *Nano letters*, 5(2):373–377, 2005.
- Michael Waldow, Tobias Plötzing, Martin Gottheil, Michael Först, Jens Bolten, Thorsten Wahlbrink, and Heinrich Kurz. 25ps all-optical switching in oxygen implanted silicon-on-insulator microring resonator. *Optics Express*, 16(11):7693–7702, 2008.
- Graham T Reed, Milan M Milosevic, Xia Chen, and David J Thomson. Trimming of ring resonators via ion implantation in silicon. In *Integrated Optics: Physics and Simulations III*, volume 10242, pages 128–133. SPIE, 2017.
- Milan M Milosevic, Xia Chen, Wei Cao, Antoine FJ Runge, Yohann Franz, Callum G Littlejohns, Sakellaris Mailis, Anna C Peacock, David J Thomson, and Graham T Reed. Ion implantation in silicon for trimming the operating wavelength of ring resonators. *IEEE Journal of Selected Topics in Quantum Electronics*, 24(4):1–7, 2018.
- J J Ackert, J K Doylend, D F Logan, P E Jessop, R Vafaei, L Chrostowski, and A P Knights. Defect-mediated resonance shift of silicon-on-insulator racetrack resonators. *Optics Express*, 19(13):11969–11976, 2011.
- David E Hagan, Benjamin Torres-Kulik, and Andrew P Knights. Post-fabrication trimming of silicon ring resonators via integrated annealing. *IEEE Photonics Technology Letters*, 31(16):1373–1376, 2019.
- J W Mayer, L. Eriksson, and J A Davies. *Ion Implantation in Semiconductors: Silicon and Germanium*. Academic Press, New York, 1970.
- Osamah Abdullah S Alsaman. *Silicon Photonics Platforms for Sensing and Telecoms*. PhD thesis, The University of Manchester (United Kingdom), 2021.

## Supplementary information

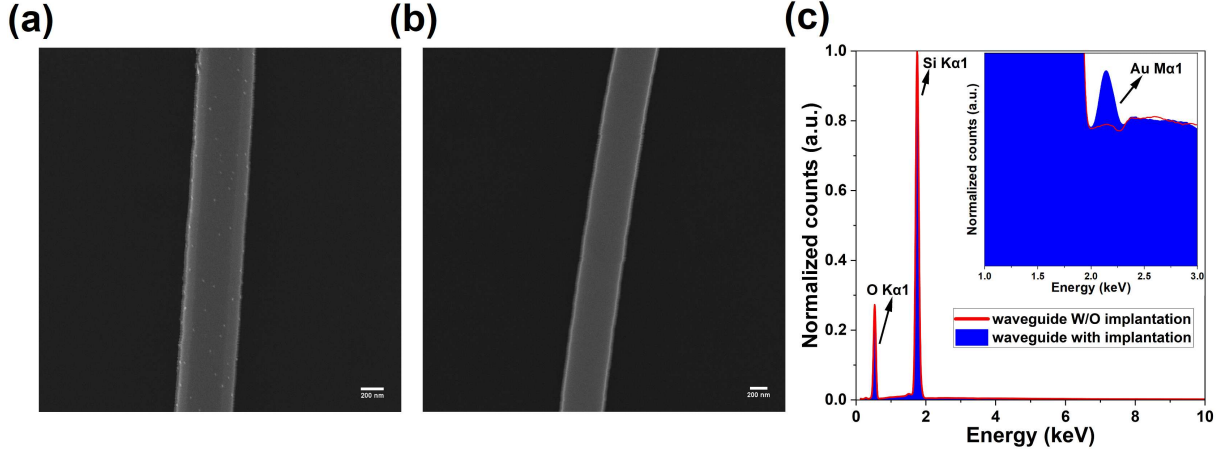


Figure S1: Post-annealing (500 °C) secondary electron images of waveguides (a) following  $5 \times 10^{15} \text{ cm}^{-2}$  gold implantation, (b) without gold implantation. (c) EDS spectra of the devices mentioned in (a) and (b) showing clear increase in Au signal in the implanted device.

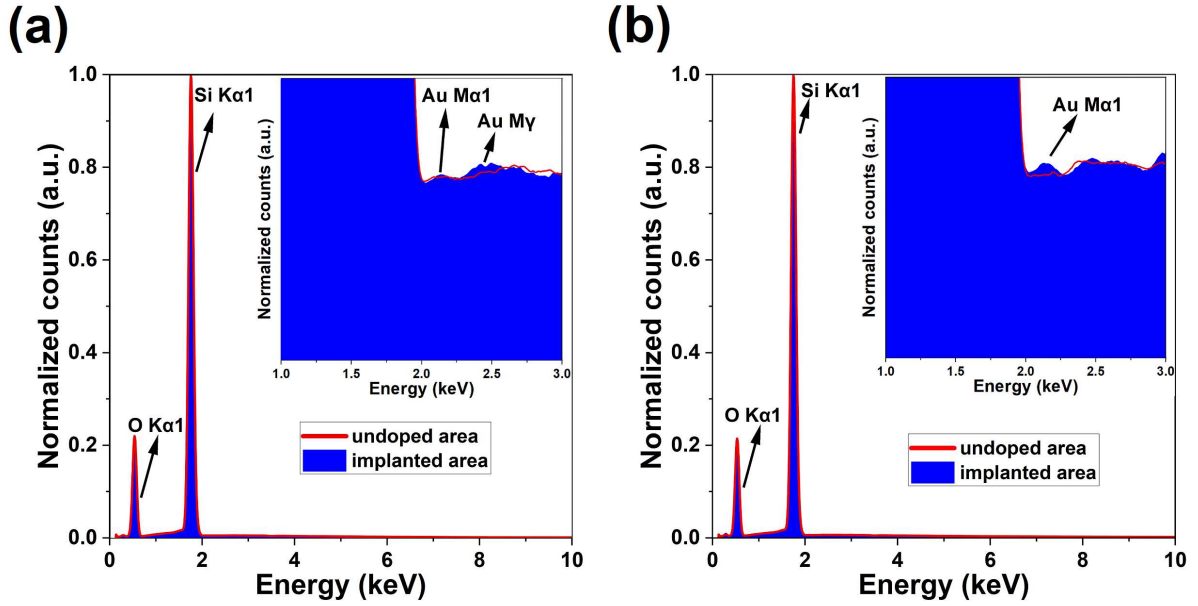
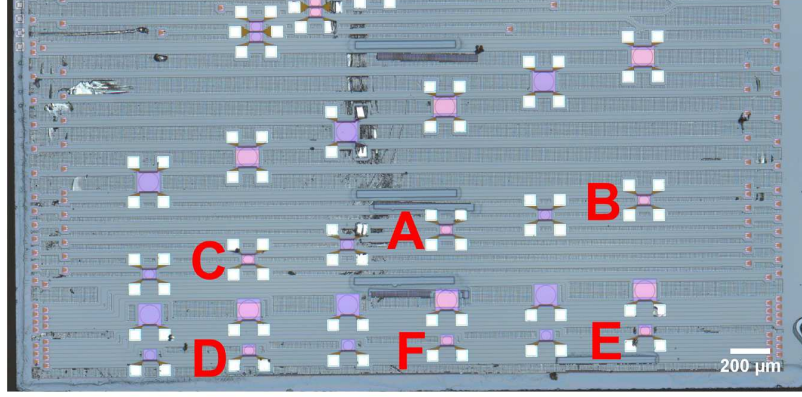
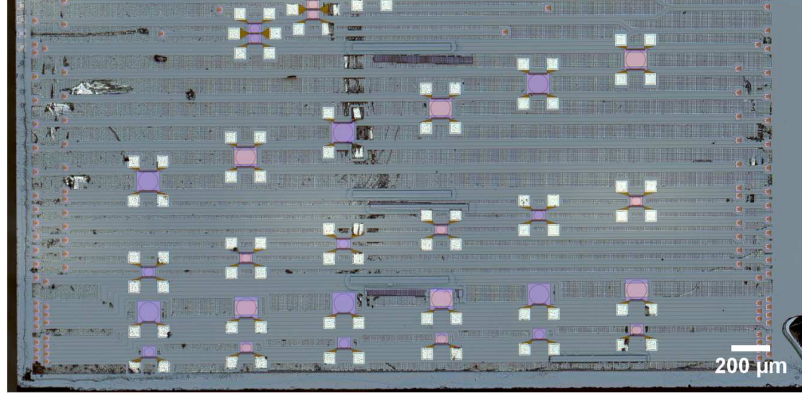


Figure S2: Post-annealing EDS spectra for the unimplanted and Au implanted areas of (a) device B, (b) device E.

(a)



(b)



(c)

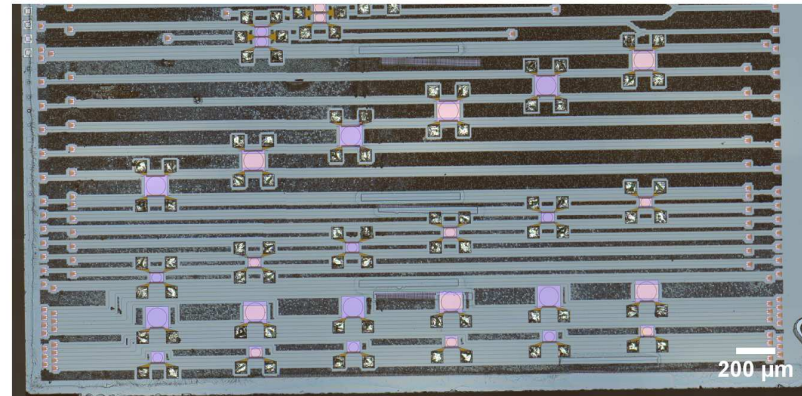


Figure S3: Optical images of the photonic chip showing devices studied, labeled to the left of each MRR. (a) Image taken prior to implantation. (b) Image taken following implantation (except reference devices A and D) and a series thermal anneals from 500 °C to 650 °C. (c) Image taken following a further anneal at 700 °C. In (c) it can be observed that the chip has been thermally damaged by the contrasting dark regions with respect to (a) and (b).